

Singular spectrum analysis and its applications in mapping mantle seismic structure

Ramin M.H. Dokht, Yu Jeffrey Gu and Mauricio D. Sacchi

Department of Physics, University of Alberta, Edmonton, AB T6G2E1, Canada. E-mail: ramin1@ualberta.ca

Accepted 2016 December 16. Received 2016 December 14; in original form 2016 July 18

SUMMARY

Seismic discontinuities are fundamental to the understanding of mantle composition and dynamics. Their depths and impedance contrasts are generally determined using secondary phases such as SS precursors and P -to- S converted waves. However, analysing and interpreting these weak signals often suffer from incomplete data coverage, high noise levels and interfering seismic arrivals, especially near tectonically complex regions such as subduction zones. To overcome these pitfalls, we adopt a singular spectrum analysis (SSA) method to remove random noise, reconstruct missing traces and enhance the robustness of SS precursors and P -to- S conversions from mantle seismic discontinuities. Our method takes advantage of the predictability of time series in the frequency–space domain and performs rank reduction using a singular value decomposition of the trajectory matrix. We apply SSA to synthetic record sections as well as the observations of (1) SS precursors beneath the northwestern Pacific subduction zones, and (2) P -to- S converted waves from southwestern Canada. In comparison with raw or interpolated data, the SSA enhanced seismic sections exhibit greater resolution due to the suppression of random noise (which reduces signal amplitude during standard averaging procedures) through rank reduction. SSA also enables an effective separation of the SS precursors from the postcursors of S-wave core diffractions. This method will greatly benefit future analyses of weak crustal and mantle seismic phases, especially when data coverages are less than ideal.

Key words: Time-series analysis; Fourier analysis; Mantle processes; Phase transitions; Body waves; Subduction zone processes.

1 INTRODUCTION

Enhancement of the signal of interest and suppression of random noise are crucial for achieving superior image quality and signal coherency (Crozat 1988; Sacchi 2009; Orosez & Sacchi 2011; Naghizadeh 2012). Over the past decades, different methods have been proposed for data interpolation and noise attenuation by exploring the predictability of seismic signals. These methods may be performed in the time–space (t – x) domain (Abma & Claerbout 1995) or by transforming the data to other domains such as frequency–space (Canales 1984; Gulunay 1986; Spitz 1991), slant-stack (also known as Radon domain; Sacchi & Ulrych (1995); Trad *et al.* (2002)), and frequency–wavenumber (Naghizadeh 2012). A method that has received significant recent attention is singular spectrum analysis (SSA), a rank reduction-based technique (also known as Cadzow filtering) for the simultaneous random noise removal and data reconstruction in the case of missing samples (Broomhead & King 1986; Cadzow 1988; Sacchi 2009; Orosez & Sacchi 2011). This technique was first introduced in time domain in the analyses of experimental dynamical systems (Broomhead & King 1986; Fraedrich 1986) in the 1980s. It was later adapted to

the frequency–space (f – x) domain and relied on the separation between coherent, linear signals and incoherent noise (Cadzow 1988; Trickett 2003; Orosez & Sacchi 2011; Yuan & Wang 2011). This algorithm is predicated on the analysis of eigen/singular values but incorporates additional phase or spatial information (Golub & Van Loan 1996; Trickett 2008; Sacchi 2009). To date, SSA has found successful applications in climatology/meteorology (Vautard & Ghil 1989; Ghil *et al.* 2002), astronomy (Auvergne 1988; Varadi *et al.* 1999), and economic data series analysis (Hassani & Thomakos 2010; Kumar & Jain 2010).

Despite well-documented successes in seismic data processing (Trickett & Burroughs 2009; Orosez & Sacchi 2011; Chen & Sacchi 2015), applications of SSA are rare in the analysis of earthquake records (Gu *et al.* 2015) and the potential of this method has not been fully recognized. In this study, we present the basic theory behind SSA and apply the SSA interpolation (an open source Julia-based package) to mantle seismic imaging. The merits of this method are demonstrated through high-frequency P -to- S conversions (Vinnik 1977; Dueker & Sheehan 1997; Rondenay 2009) and long-period shear wave reflections (Shearer 1993; Gu *et al.* 1998; Deuss 2009) from mantle discontinuities, both of which are known

to suffer from low signal-to-noise ratios (SNRs) and gaps in data coverage.

2 THEORY

We apply SSA, a frequency domain noise attenuation technique, to increase the coherency of conversions or reflections from upper mantle seismic discontinuities. SSA is a model-free method that uses singular value decomposition (SVD) to reduce the rank of the Hankel matrix (Golyandina *et al.* 2001; Sacchi 2009). To do so, we first represent seismic events ($d(t, x)$) in a time–space (t – x) matrix

$$\mathbf{d} = \begin{pmatrix} d_{1,1} & d_{1,2} & \cdots & d_{1,n} \\ d_{2,1} & d_{2,2} & \cdots & d_{2,n} \\ \vdots & \vdots & \ddots & \vdots \\ d_{m,1} & d_{m,2} & \cdots & d_{m,n} \end{pmatrix} \quad (1)$$

where $d_{j,i}$ corresponds to the j th sample of the i th trace of the data matrix composed of m samples in each seismogram for n total traces. The data in the t – x domain is then transformed to the f – x domain by taking the Fourier transform of each seismogram with respect to time. The f – x transformed data matrix is now

$$\mathbf{D} = \begin{pmatrix} D_{1,1} & D_{1,2} & \cdots & D_{1,n} \\ D_{2,1} & D_{2,2} & \cdots & D_{2,n} \\ \vdots & \vdots & \ddots & \vdots \\ D_{M,1} & D_{M,2} & \cdots & D_{M,n} \end{pmatrix}, \quad (2)$$

where $D_{j,i}$ corresponds to the j th frequency sample of the i th trace. A related trajectory matrix, that is, the Hankel matrix where each skew-diagonal is constant, can be constructed at a fixed frequency f_j as (Sacchi 2009):

$$\mathbf{M}(f_j) = \begin{pmatrix} D_{j,1} & D_{j,2} & \cdots & D_{j,K} \\ D_{j,2} & D_{j,3} & \cdots & D_{j,K+1} \\ \vdots & \vdots & \ddots & \vdots \\ D_{j,L} & D_{j,L+1} & \cdots & D_{j,n} \end{pmatrix}. \quad (3)$$

In this expression L and K are chosen to be $\lfloor n/2 \rfloor + 1$ and $n - L + 1$, respectively, to approximate the Hankel matrix as a square matrix (Trickett & Burroughs 2009; Orosez & Sacchi 2011). In the presence of a linear event, it can be shown that

$$D_{j,n} = (e^{-i2\pi f_j p \Delta x}) D_{j,n-1}, \quad (4)$$

where p is the ray parameter and Δx is the distance between two adjacent traces. In other words, for equally spaced traces, the event becomes linearly predictable in the spatial direction (Sacchi 2009)

and the rank of the Hankel matrix equals to 1. Eq. (3) can be written in a reduced-rank form as (Sacchi 2009):

$$\mathbf{M}(f_j) = \begin{pmatrix} D_{j,1} & WD_{j,1} & \cdots & W^{K-1} D_{j,1} \\ D_{j,2} & WD_{j,2} & \cdots & W^{K-1} D_{j,2} \\ \vdots & \vdots & \ddots & \vdots \\ D_{j,L} & WD_{j,L} & \cdots & W^{K-1} D_{j,L} \end{pmatrix}, \quad (5)$$

where $W = e^{-i2\pi f_j p \Delta x}$. For the input data, $d(t, x)$ consists of k linear events and the transformed data $D(f, x)$ contain k complex sinusoids. Consequently, the rank of the Hankel matrix constructed from the transformed data at each frequency is equal to k (Yang & Hua 1996; Orosez & Sacchi 2011). The rank of the trajectory matrix increases with noise and the number of missing traces (Sacchi 2009; Chen & Sacchi 2015). Furthermore, the SSA filter relies on the approximation of the Hankel matrix by another matrix of a lower rank (Golyandina *et al.* 2001). Assuming that the signal is linearly predictable in space (Orosez & Sacchi 2011; Yuan & Wang 2011), rank reduction techniques can be applied to the Hankel matrix, \mathbf{M} , to (1) separate the random noise from coherent events and (2) reconstruct the missing observations by reducing the rank of the Hankel matrix. Subsequently, the low rank approximation of the Hankel matrix can be estimated using SVD (Freire & Ulrych 1988):

$$\hat{\mathbf{M}}(f_j) = \mathbf{U}_k \mathbf{S}_k \mathbf{V}_k^H, \quad (6)$$

where \mathbf{S}_k represents a diagonal matrix containing the k largest singular values of the Hankel matrix \mathbf{M} sorted in descending order, and \mathbf{U}_k and \mathbf{V}_k are the associated eigenvectors of $\mathbf{M}(f_j)$ (Trickett 2003). While the low-rank matrix $\hat{\mathbf{M}}(f_j)$ is not a Hankel matrix and the structure of the original trajectory matrix is generally not preserved (Chen & Ma 2014), one can obtain the closest approximation to the Hankel matrix by averaging the anti-diagonal elements of each low rank trajectory matrix, $\hat{\mathbf{M}}(f_j)$, and reconstruct the i th row of the transformed data in the f – x domain. The aforementioned process is carried out for all frequencies f_j in the band of the seismic signal. Finally, an enhanced seismic image is obtained by transforming data back to the t – x domain. An iterative algorithm similar to the one suggested by Orosez & Sacchi (2011) is used to recover the true amplitudes of the missing traces:

$$\mathbf{D}_i = \alpha \mathbf{D}_{\text{obs}} + (1 - \alpha \mathbf{T}) F_{\text{SSA}}[\mathbf{D}_{i-1}], \quad i = 1, 2, 3, \dots, \text{itr}_{\max}. \quad (7)$$

In this equation, \mathbf{D}_i and \mathbf{D}_{i-1} are the interpolated data in the current and previous iterations, respectively, and \mathbf{D}_{obs} denotes the input data matrix with missing observations. The operator \mathbf{T} is a sampling matrix (with the size of the original data), within which the elements equal to 1.0 (where data exist) or 0.0 (otherwise). The operator F_{SSA} represents the SSA filter and the denoising parameter α is a scalar (between 0 and 1) associated with the noise level. F_{SSA} is

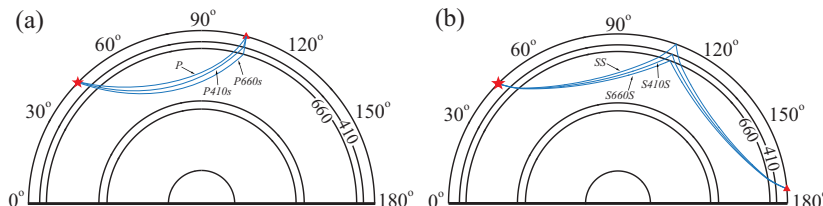


Figure 1. (a) Theoretical ray paths of P and P -to- S conversions at a 60° epicentral distance. (b) Ray paths of SS and its precursors at 130° distance. These ray paths are computed using PREM (Dziewonski & Anderson 1981). The stars and triangles denote the earthquake and seismic station locations, respectively.

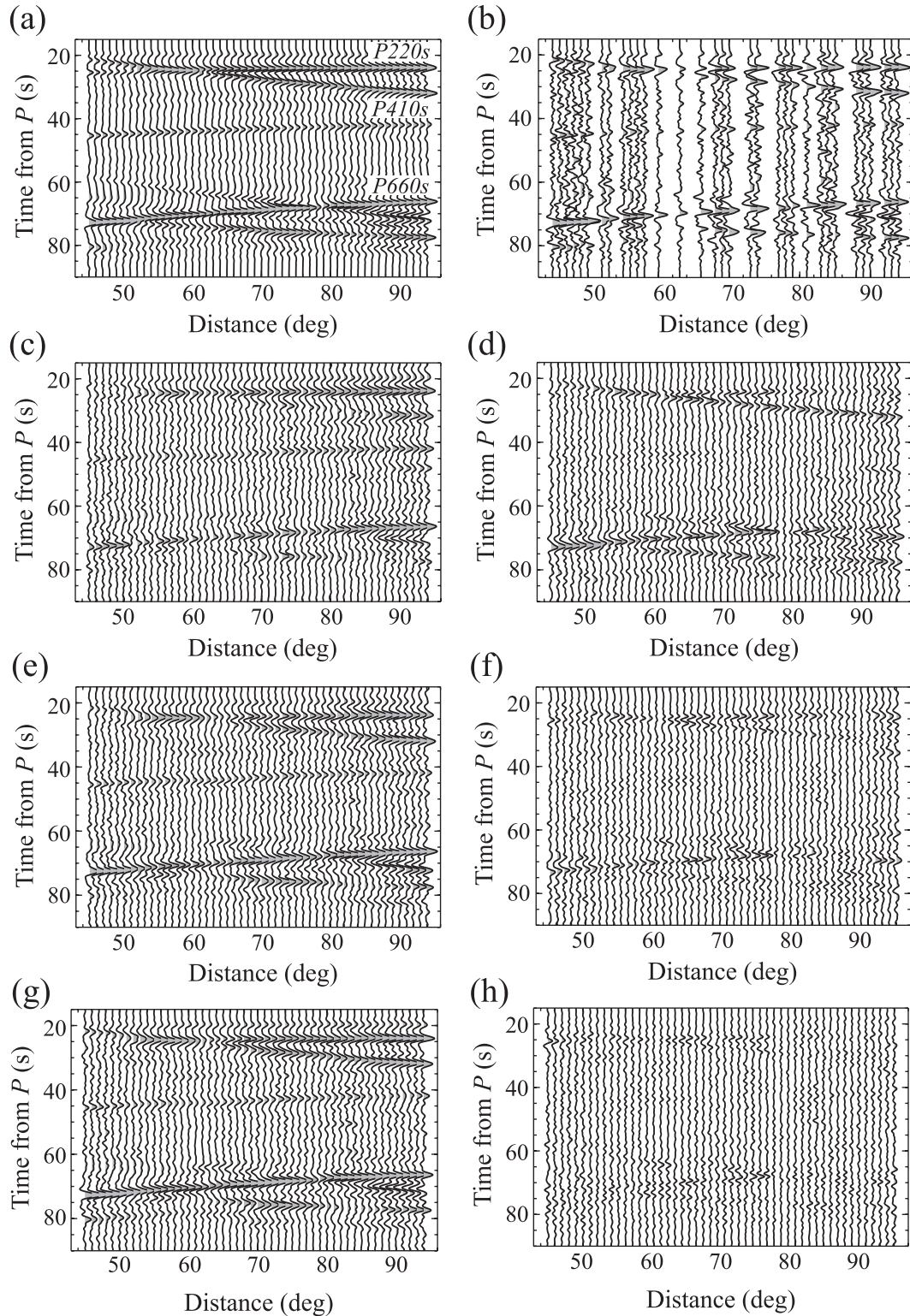


Figure 2. Application of SSA on a decimated record section of synthetic receiver functions contaminated with random noise. (a) Original data. (b) Noise-added data decimated to ~ 70 per cent of the original number of traces. (c,e,g) Results of SSA filtering at k values of 1, 2 and 3, respectively. (d,f,h) The corresponding differences between the reconstructed (c, e, g) and original (a) data.

formed by concatenating the following operators: data Hankelization, rank-reduction and antidiagonal averaging. Finally, because a true amplitude recovery is usually not achievable after a single iteration, we employ an iterative algorithm that terminates when the

maximum number of iterations itr_{max} is reached or when the normalized error function $\|\mathbf{D}_i - \mathbf{D}_{i-1}\|^2 / \|\mathbf{D}_{i-1}\|^2 < \epsilon$ with $\epsilon = 10^{-6}$. Examples of SSA in mantle interface analysis will be provided in Section 3.

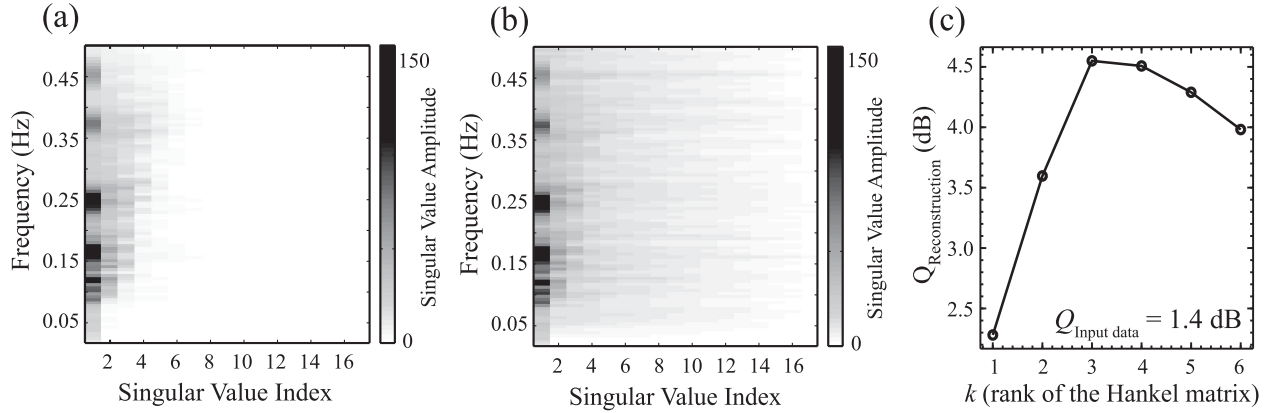


Figure 3. Distributions of singular values for (a) noise-free synthetic receiver functions and (b) noise-added, decimated data presented in Fig. 2. (c) Quality of the reconstruction (Q) versus the rank of the Hankel matrix (k). The input data show a Q value of 1.4 dB. The maximum value of Q is achieved at $k = 3$.

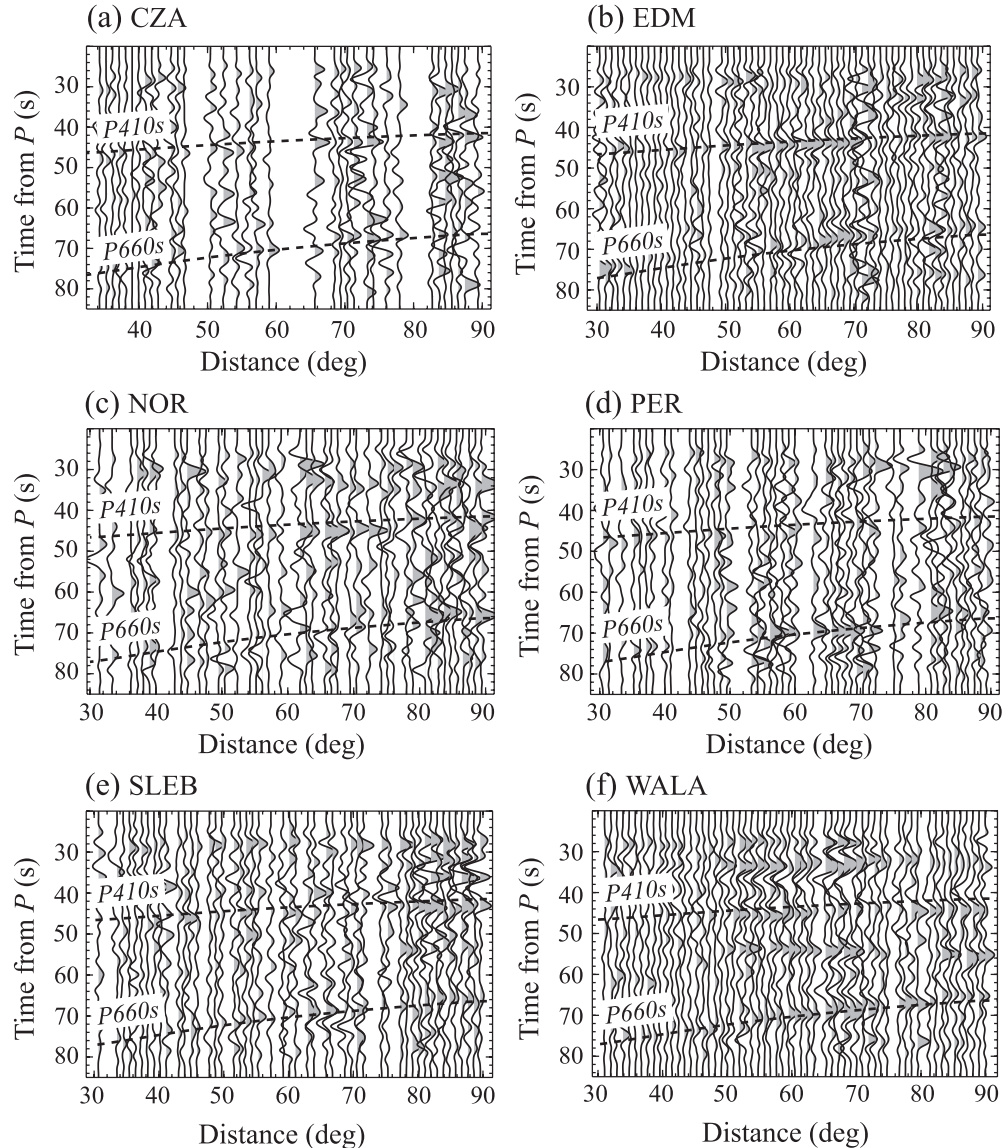


Figure 4. Partially stacked radial receiver functions calculated for six seismic stations in southwestern Canada. Approximately 40 per cent, 2 per cent, 30 per cent, 25 per cent, 21 per cent and 3 per cent of data are missing at stations CZA, EDM, NOR, PER, SLEB and WALA, respectively. The dashed lines indicate the PREM predicted differential traveltimes of $P410s$ - P and $P660s$ - P (Dziewonski & Anderson 1981).

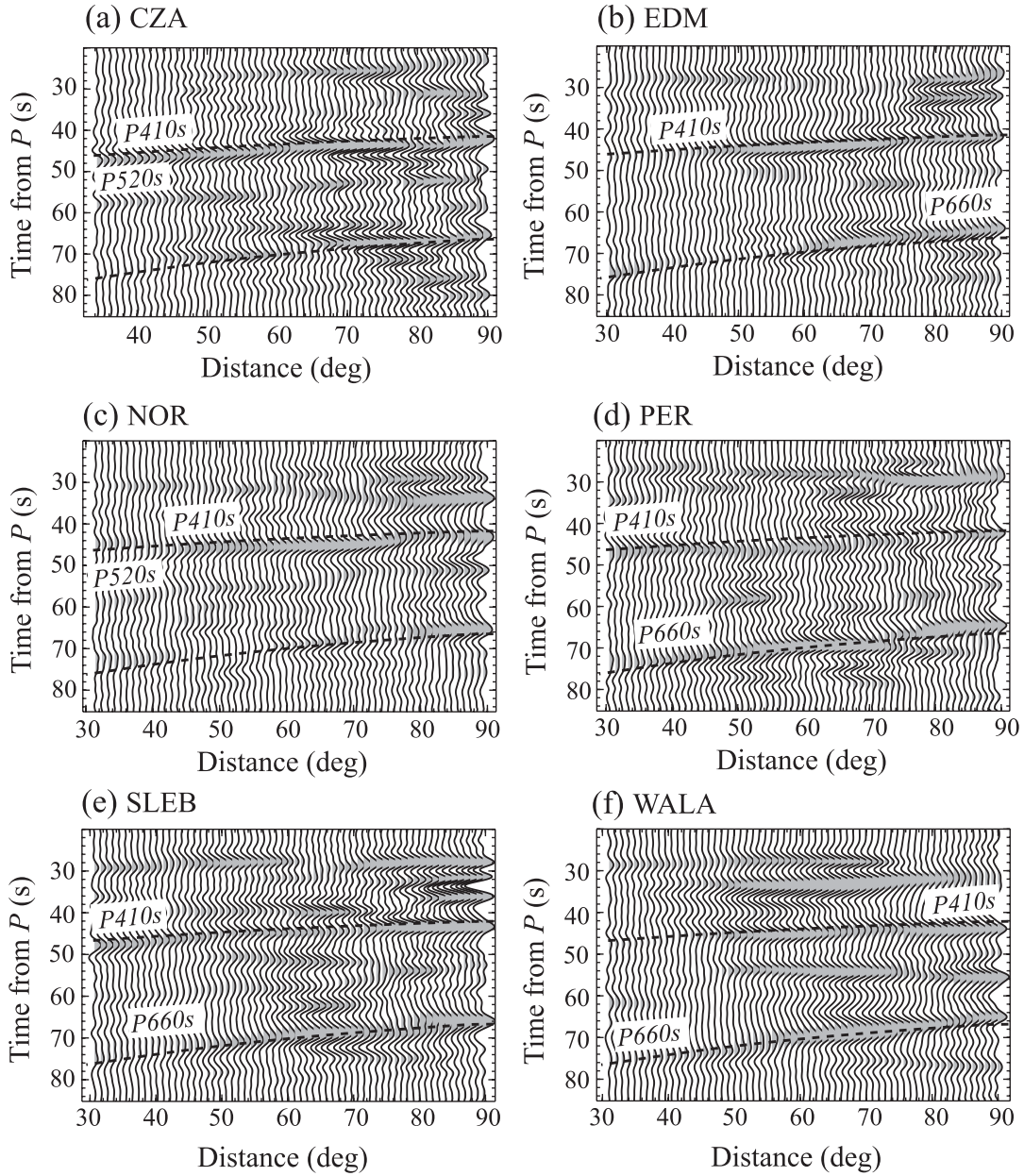


Figure 5. Reconstructed and spatially resampled receiver functions by applying the SSA interpolation. SSA is designed to reduce the rank of the Hankel matrix to 3. The dashed lines indicate the PREM predicted differential traveltimes of $P410s$ - P and $P660s$ - P (Dziewonski & Anderson 1981).

3 APPLICATION

A wide range of secondary seismic arrivals has been utilized to determine the structure surrounding mantle seismic discontinuities. Two prominent examples are P -to- S converted waves, often calculated from ‘receiver functions (RFs)’ (Ammon *et al.* 1990; Kind *et al.* 1996; Ligorria & Ammon 1999; Lawrence & Shearer 2006; Rondenay 2009; Chen *et al.* 2015), and long-period SS precursors (Shearer & Masters 1992; Flanagan & Shearer 1998; Gu *et al.* 1998; Deuss & Woodhouse 2002; Houser *et al.* 2008; Fig. 1). The former phase group is usually examined at high frequencies, targeting the seismic structures beneath the receiver (Cassidy 1995; Song *et al.* 2004; Schaeffer & Bostock 2010; Gu *et al.* 2015) or source (Wicks & Richards 1993; Castle & Creager 2000) location. In comparison, SS precursors are ‘global phases’ less dependent on

path geometries (Shearer & Masters 1992; Gu *et al.* 1998; Zheng *et al.* 2015). Results from these two approaches are generally complementary, especially in major subduction zones (Li *et al.* 2000; Gu & Dziewonski 2002; Lawrence & Shearer 2006). The section below investigates the effectiveness of SSA in the waveform analyses of RFs and SS precursors for the imaging of mantle transition zone (MTZ) discontinuities (Ringwood 1975; Dziewonski & Anderson 1981).

3.1 P -to- S receiver function

RF analyses have been widely conducted to determine the properties of upper mantle interfaces (Vinnik 1977; Langston 1979; Lawrence & Shearer 2006; Tauzin *et al.* 2008; Schaeffer & Bostock 2010;

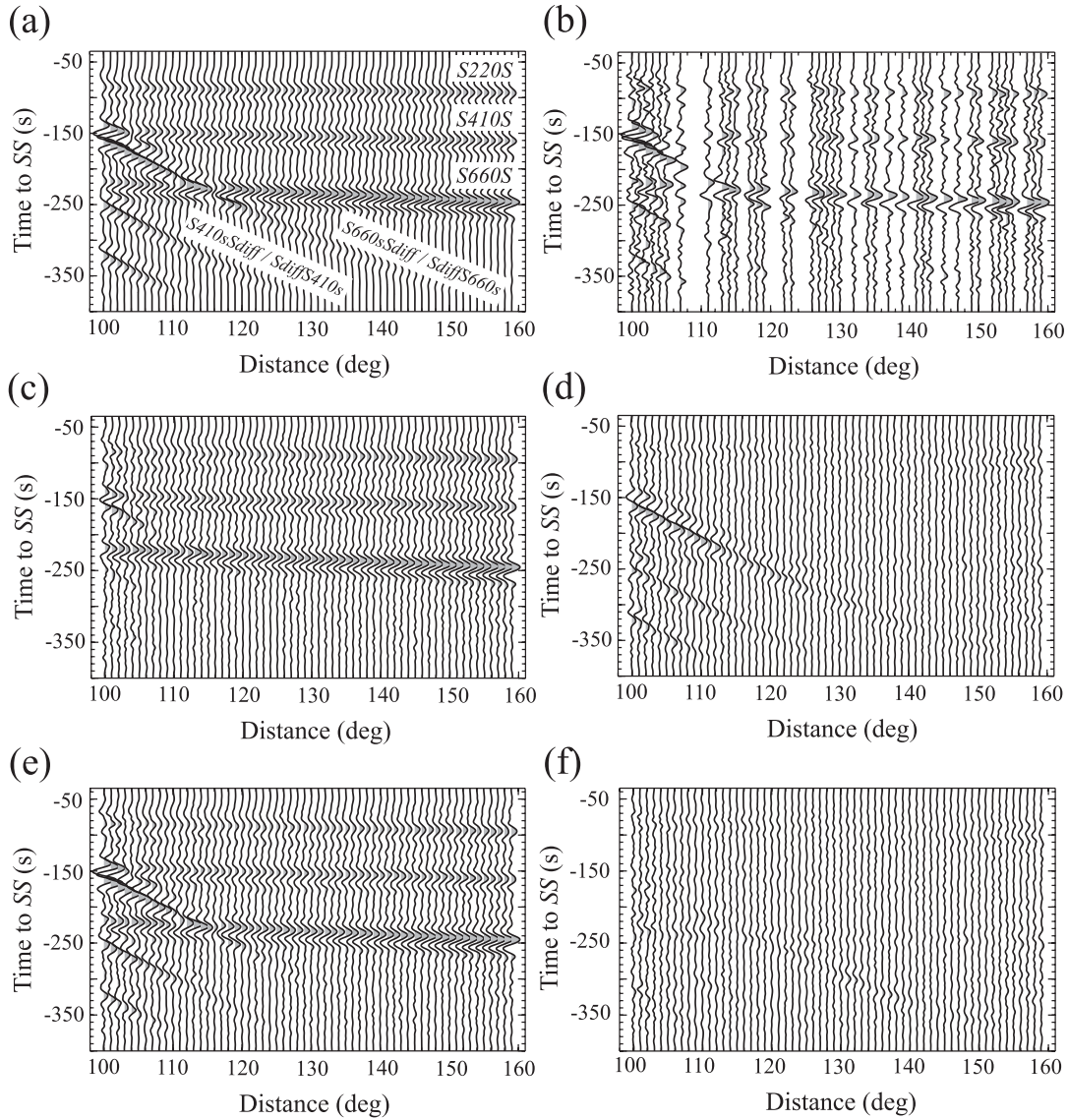


Figure 6. Application of SSA on synthetic SS precursor waveforms contaminated with random noise. (a) Noise-free synthetic records. (b) Noise-added data with 30 per cent of the traces randomly removed. (c,e) Reconstructed data from (b) using $k = 1$ and 2, respectively. (d,f) Differences between the reconstructed data (c,e) and the original input waveforms (a).

Gu *et al.* 2015). The primary conversions from mantle discontinuities are often difficult to identify due to low SNR and potential effects of multiple reverberations or interfering phases (Schaeffer & Bostock 2010). Hence, stacking is generally performed to enhance the SNR and reduce the random noise, but its effectiveness can be compromised under severe noise levels and/or a non-Gaussian noise distributions. Fig. 2(a) shows a record section of synthetic RFs containing P -to- S converted phases from mantle interfaces, calculated using a propagator matrix approach (Kennett 1983; Shearer 2009) based on PREM (Dziewonski & Anderson 1981) for source-receiver distances ranging from 45 to 95 degrees. After normalizing and aligning each seismogram by its peak amplitude, the move-out of the converted phases becomes approximately linear across the record section. We then decimate the data by randomly removing 34 per cent of the traces and contaminate the selected records with 10 per cent Gaussian noise (Fig. 2b). A comparison between the

reconstructed data (Figs 2c–h) suggests that the best performance of the SSA interpolation is achieved using the 3 largest singular values; in other words, the optimal desired rank of the Hankel matrix is $k = 3$. On the other hand, the presence of random noise increases the non-zero singular values of the trajectory matrix (Figs 3a and b). To assess the quality of the reconstructions for different ranks, we define

$$Q = 10 \log \frac{\|\mathbf{d}_0\|^2}{\|\mathbf{d}_0 - \hat{\mathbf{d}}\|^2} \quad (8)$$

where \mathbf{d}_0 and $\hat{\mathbf{d}}$ denote the noise-free and reconstructed data, respectively, in the t - x domain. By this definition, Q approaches infinity in the case of perfect data reconstruction. In this experiment, the calculated Q values for the interpolated data using rank $k = 1, 2$ and 3 are 2.3, 3.6 and 4.6 dB, respectively, suggesting that the highest quality of reconstruction is achieved when $k = 3$. Further increases

Table 1. Polynomial Coefficients of linear and parabolic regressions of SdS traveltimes and path functions using PREM (Dziewonski & Anderson 1981) and IASP91 (Kennett & Engdahl 1991). The coefficients p_0 , p_1 and p_2 are sorted in an ascending order, that is, SdS differential times are calculated as $p_0 + p_1x + p_2x^2$ (where x represents the source-receiver distance in degrees). The coefficient of determination, R^2 , indicates the goodness of fit of each trajectory. R^2 is the normalized variance reduction (Gu & Shen 2015) that reflects the performance of the regression curve in predicting the variations in the original data.

		PREM				IASP91			
		p_0	p_1	p_2	R^2	p_0	p_1	p_2	R^2
<i>S410S</i>	Linear	-120.8	-0.2523	0.0	0.9988	-123.5	-0.2588	0.0	0.999
	Parabolic	-111.6	-0.3956	0.00055	1.0	-114.9	-0.3947	0.000523	1.0
<i>S660S</i>	Linear	-169.7	-0.4887	0.0	0.9985	-167.9	-0.479	0.0	0.9987
	Parabolic	-149.6	-0.8035	0.00121	1.0	-150.0	-0.7606	0.00108	1.0

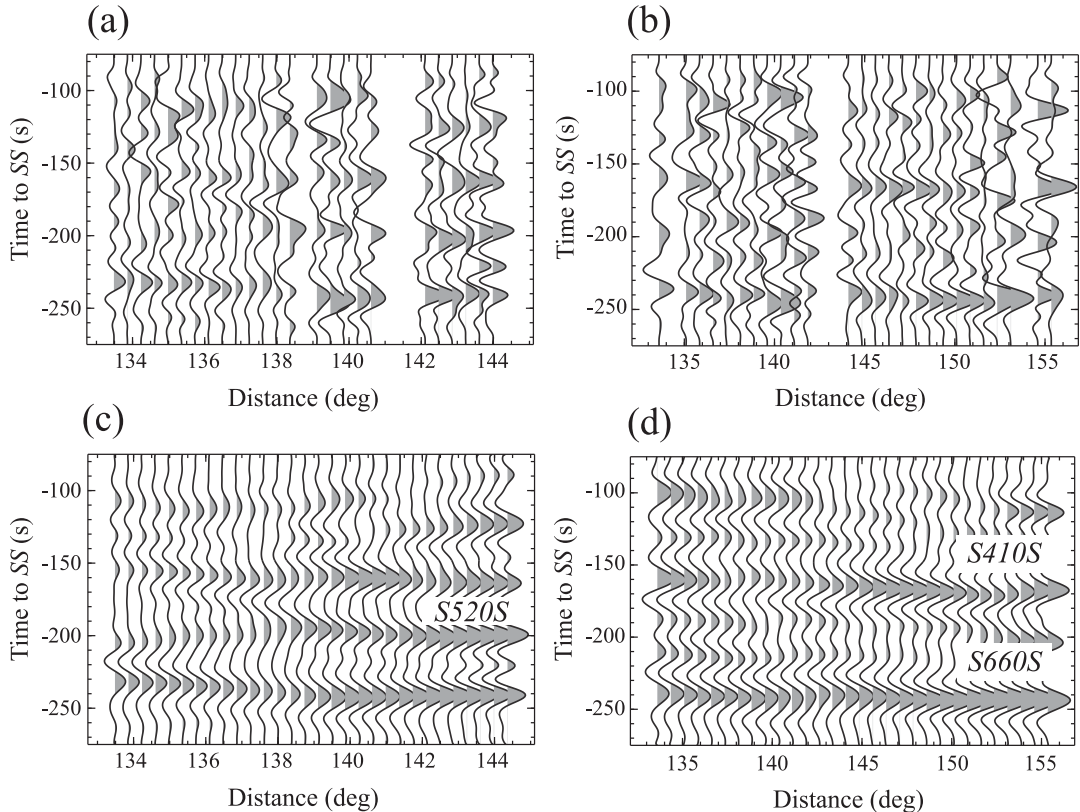


Figure 7. (a,b) Partially stacked SS precursor waveforms sampling the upper mantle beneath the Wudalianchi hotspot in northeastern China. The running average window sizes are 0.5° and 1.0° , respectively, for (a) and (b) with 25 per cent overlaps among the adjacent windows. (c,d) Reconstructed SS precursor waveforms from (a) and (b), respectively, using $k = 2$.

of rank k lead to systematic decreases in Q due to the elevated levels of recovered noise in the data (Fig. 3c).

In the second experiment, we utilize a data set of 1563 high-quality RFs, collected from six broad-band, three-component seismic stations from the Canadian Rockies and Alberta Network (CRANE; Gu *et al.* (2011)) and Canadian National Seismograph Network (CNSN). This data set has been previously examined by Gu *et al.* (2015) to map the mantle stratigraphy beneath the Western Canada Sedimentary Basin (WCSB). The availability of the published results enables us to quantitatively assess the performance of SSA in noise reduction and reflectivity imaging. We group the RFs into common receiver gathers and sort them by source-receiver distances. The resulting source-receiver distances are not regularly spaced, which do not satisfy the spatial sampling requirement of SSA (Oropeza & Sacchi 2011). Hence, prior to SSA, we partially stack the traces using a 1-degree running average window. Figs 4 and 5 show the comparison between the raw RFs and the

reconstructed data using the SSA interpolation. The rank of the trajectory matrix, k , is determined based on the synthetic experiments and the number of expected linear arrivals in the data section. The input partial stacks (especially those observed at the stations CZA, NOR, PER and SLEB) show no discernible mantle conversions due to low SNRs and gaps in the sections of partially stacked RFs. Aside from the successful removal of data gaps, the SSA reconstruction generally enhances the signals associated with mantle conversions (i.e. $P410s$, $P660s$ and converted phases from mid-MTZ depths) while effectively reducing the random noise.

3.2 SS precursor

Similar to converted phases, the SSA algorithm can also be directly applied to the waveforms of long-period reflections from mantle interfaces. To illustrate this, we calculate a record section of 60

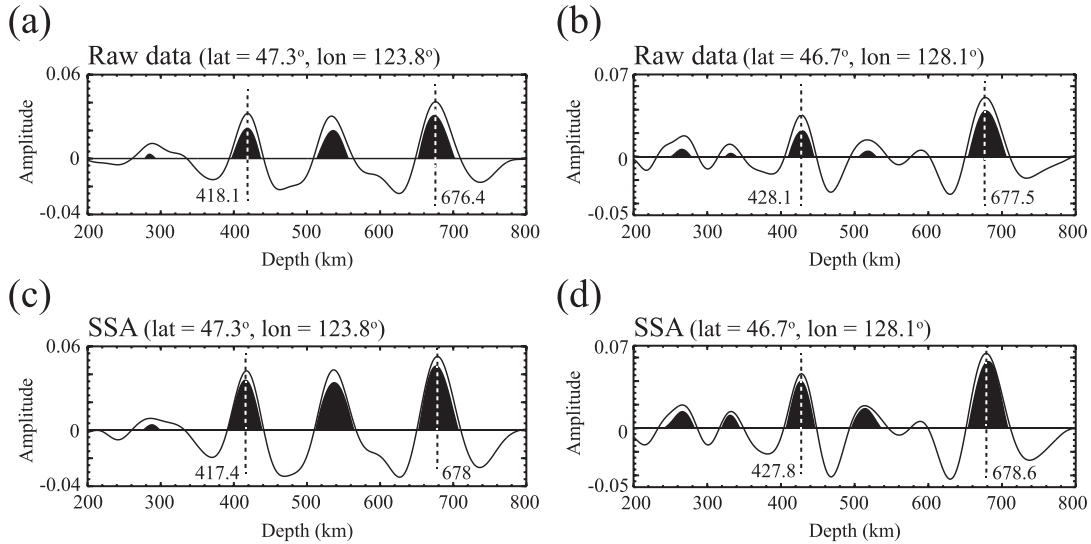


Figure 8. Stacks of depth-converted SS precursor waveforms before (panels (a) and (b)) and after (panels (c) and (d)) SSA. The stacked seismograms are calculated using the data presented in Fig. 7. The centre locations of the data gathers are as indicated. The shaded areas show the 95 per cent confidence intervals calculated using the bootstrapping resampling algorithm (Efron & Tibshirani 1990).

transverse-component seismograms with source-receiver distances ranging from 100° to 160° using PREM (Dziewonski & Anderson 1981; Fig. 6a). After the precursor (SdS) waveforms are aligned on the peak amplitudes of SS , the relative traveltimes of SS precursors can be accurately represented using parabolic functions of epicentral distance (Gu & Sacchi 2009). Based on statistical measures of the goodness of fit (which is defined as R^2 in Table 1), however, the differential traveltimes of SdS - SS can be further approximated using linear path functions (where the quadratic term is essentially zero).

In the first experiment, we randomly remove 30 per cent of traces and add 10 per cent Gaussian noise to the input section (Fig. 6b). After the SSA interpolation, the main linear arrivals (e.g. $S410S$ and $S660S$) and nearly 93 per cent of their original amplitudes are properly recovered using $k = 1$ at well sampled distances (Figs 6c and d). The topside reflections from the mantle discontinuities ($S410sSdiff/SdiffS410s$ and $S660sSdiff/SdiffS660s$, also known as $Sdiff$ postcursors (Zheng *et al.* 2015)) that interfere with SdS at distances < 130 degrees, are clearly associated with the second largest singular values of the trajectory matrix (Figs 6e and f). Unlike converted waves, only two singular values are needed to recover the key arrivals within the precursor time window.

Fig. 7 shows the SSA reconstruction of SS precursor waveforms from northeastern China. This data set was recently analysed by Dokht *et al.* (2016) in imaging the upper mantle beneath the Changbai/Wudalianchi hotspots. The input record sections (Figs 7a and b), which are obtained from partial stacking, show a series of secondary reflections (i.e. SS precursors) prior to the surface reflections. The reconstructed waveforms adequately recover the missing traces in the data gap between the 140° and 145° (Figs 7c and d). Strong signals are also observed between $S410S$ and $S660S$, in potential association with a mid-MTZ reflector near 520 km depth (see Fig. 7c; Gu *et al.* 2012). The depths of the discontinuities from the stacks of depth-converted SS precursors, calculated using the waveform data presented in Fig. 7, agree to 99 per cent before (Figs 8a and b) and after (Figs 8c and d) SSA. In comparison with stacks from the original data, SSA enhances the amplitudes of the mantle reflections by an average of 33 per cent and significantly improves their

accuracy (see Fig. 8). The reconstructed data properly recover the major depth anomalies on the discontinuities, that is, depressions of the MTZ boundaries under the Wudalianchi hotspot, that can be directly linked to the dynamic processes in association with plate convergence.

3.3 Limitation and complication

Like most noise reduction/data reconstruction methods, the effectiveness of SSA is strongly dependent on the data condition (e.g. receiver density/spacing and noise characteristics). To examine the performance of SSA in recovering missing traces, we generate a synthetic seismic section with a single linear event (Fig. 9a) and reduce the data density to 50 per cent by (1) removing every other trace (Fig. 9b) and (2) random decimation (Fig. 9c). The resulting Hankel matrix from the regularly decimated data at a constant frequency of 0.04 Hz (i.e. case 1, Fig. 9e) is of rank 2. Only the first two singular values of the Hankel matrix are non-zero, although the amplitude of largest singular value is approximately half of the original one (see Figs 9g and h). The second largest singular value at each frequency is associated with zero skew-diagonal elements of the Hankel matrix due to the alternate removal of the input traces (see Figs 9e and h). In comparison, the Hankel matrix constructed from the randomly sampled data shows a higher rank than both the original and uniformly decimated data (see Figs 9g–i). However, the Hankel matrix is less structured than the case of regular data gaps, and is therefore able to preserve the desired signal. The inability of SSA in recovering the regular data gaps is further illustrated by the results of data reconstruction (Fig. 10a). The amplitudes of the interpolated missing traces are approximately zero for all distances. In comparison, the reconstruction in the case of irregular data gaps is more accurate (Fig. 10b). A proper application of SSA on regularly decimated data will require more advanced techniques such as anti-aliasing Cadzow reconstruction (Naghizadeh & Sacchi 2013). For the majority of solid Earth applications, the SSA algorithm examined in this study is sufficient since the distributions of earthquakes and seismic stations are rarely uniform.

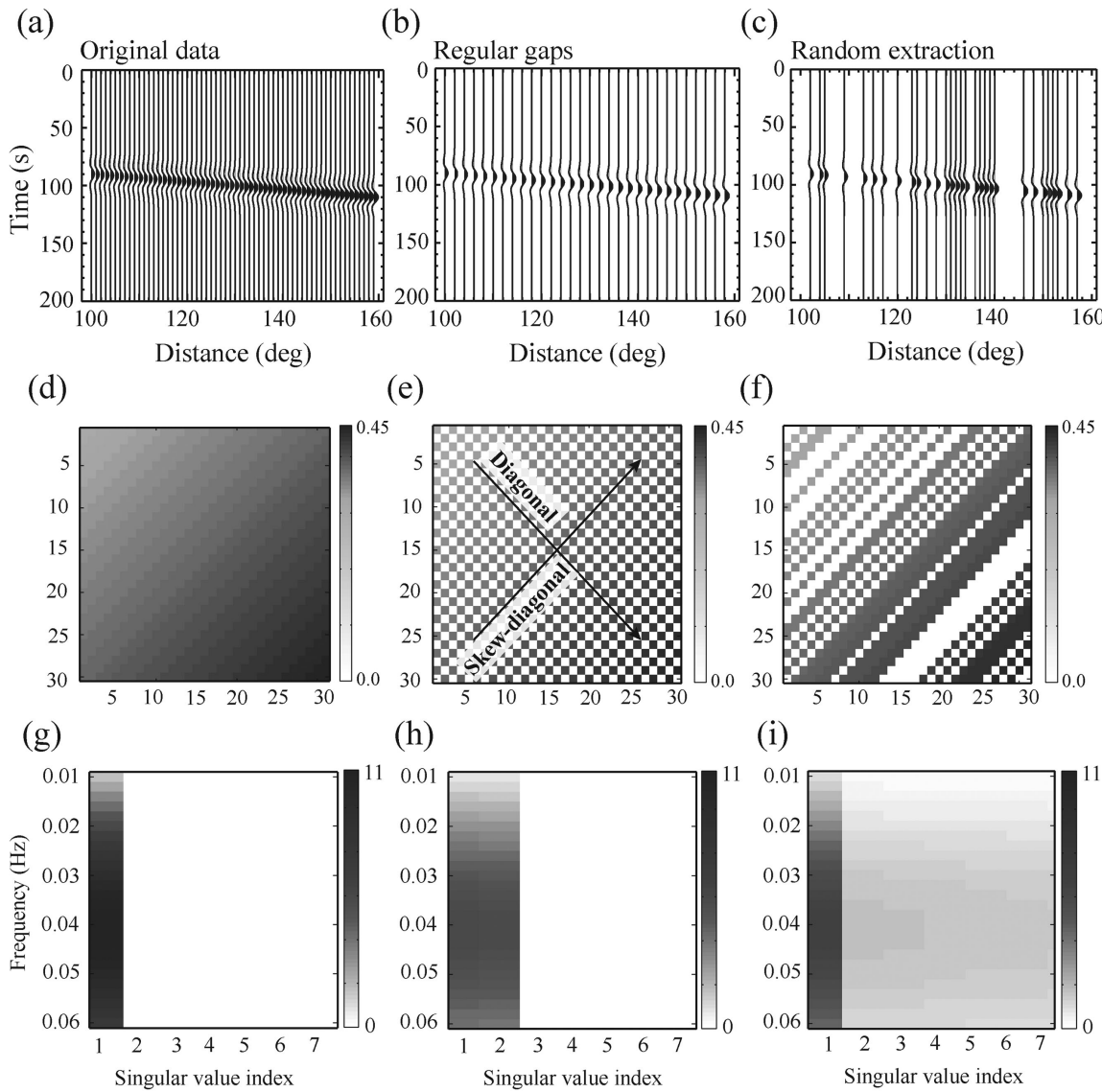


Figure 9. (a) Original data containing a linear event. (b) Modified data with regular gaps (50 per cent decimation). (c) Modified data after 50 per cent random extraction. (d–f) The corresponding Hankel matrices from (a) to (c) at 0.04 Hz frequency. (g–i) Distributions of the singular values calculated from (d) to (f).

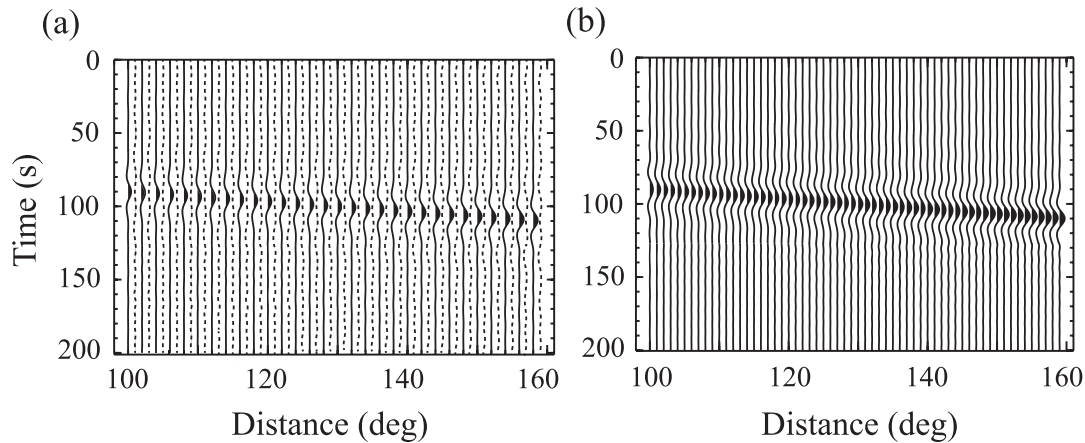


Figure 10. A comparison between the SSA interpolation results for (a) regularly and (b) randomly decimated data using $k = 1$. The dashed lines in panel (a) represent the interpolated missing traces.

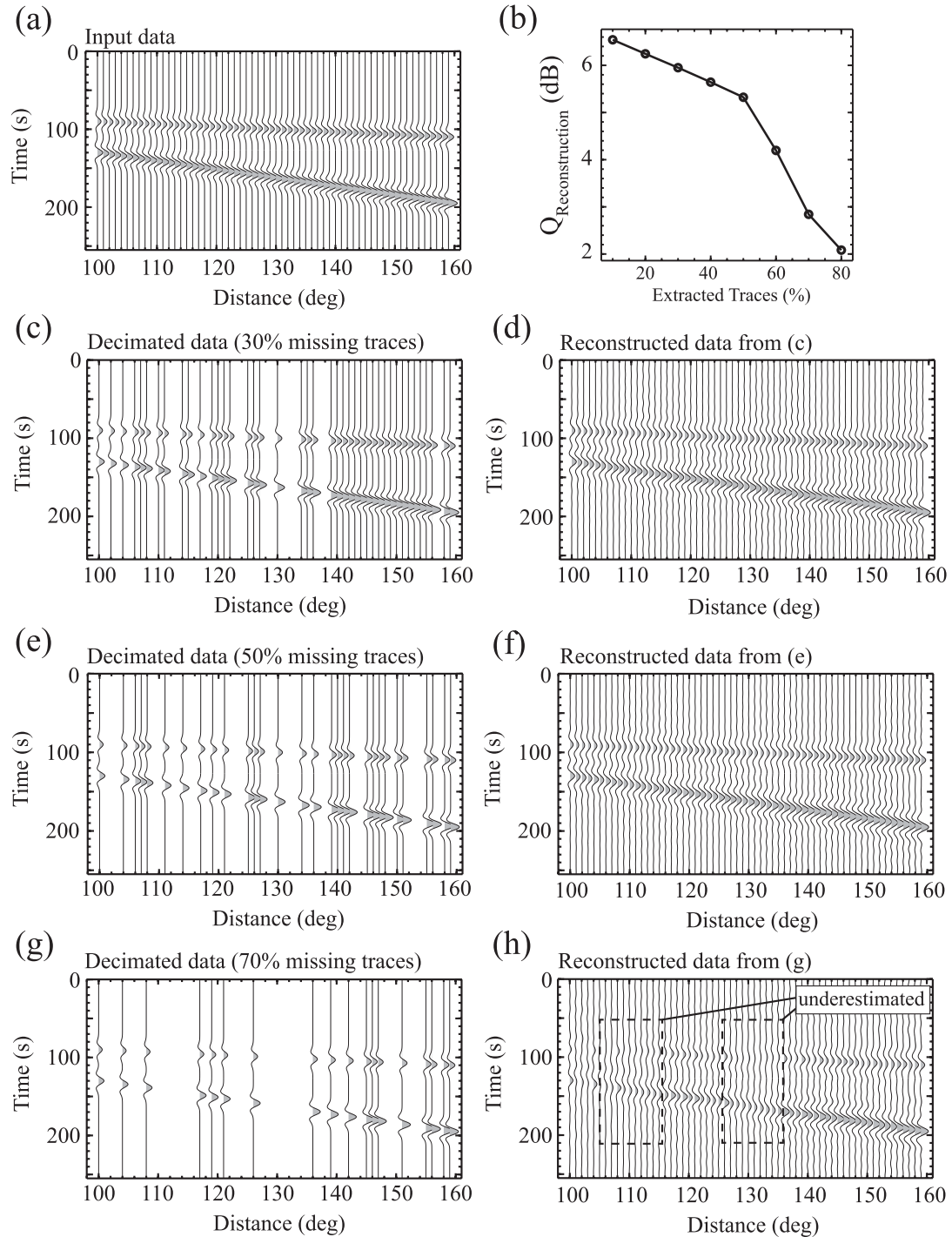


Figure 11. The effectiveness of SSA under increasing numbers of missing data traces. (a) Original data. (b) Quality of the reconstructed data versus the percentage of missing traces. (c,e,g) Input data with 30 per cent, 50 per cent and 70 per cent empty entries, respectively. (d,f,h) The corresponding interpolated data from (c), (e) and (g) using $k = 2$.

It is worth noting that the accuracy of data reconstruction is strongly dependent on the percentage of missing traces (i.e. non-regular data gaps). For a seismic section consisting of two linear arrivals (Fig. 11a), the quality of the results decreases linearly from ~ 6.5 dB at 10 per cent data gaps to ~ 5.3 dB at 50 per cent (Fig. 11b), below which the quality of the reconstruction drops off more rapidly (see Figs 11b and h). For instance, when 70 per cent of data are missing, SSA is only able to properly recover the timing of the seismic

arrivals while the amplitudes of the interpolated traces within data gaps are considerably underestimated (see Figs 11g and h).

To further quantify the performance of SSA in the presence of noise, we contaminate the synthetic section containing a single linear event (Fig. 12a) with random noise at SNR values of 1–6. In all cases, the qualities of the filtered sections are improved through the application of SSA (Figs 12b–f). The improvement in the image quality is especially significant at SNR = 1 (see Fig. 12f)

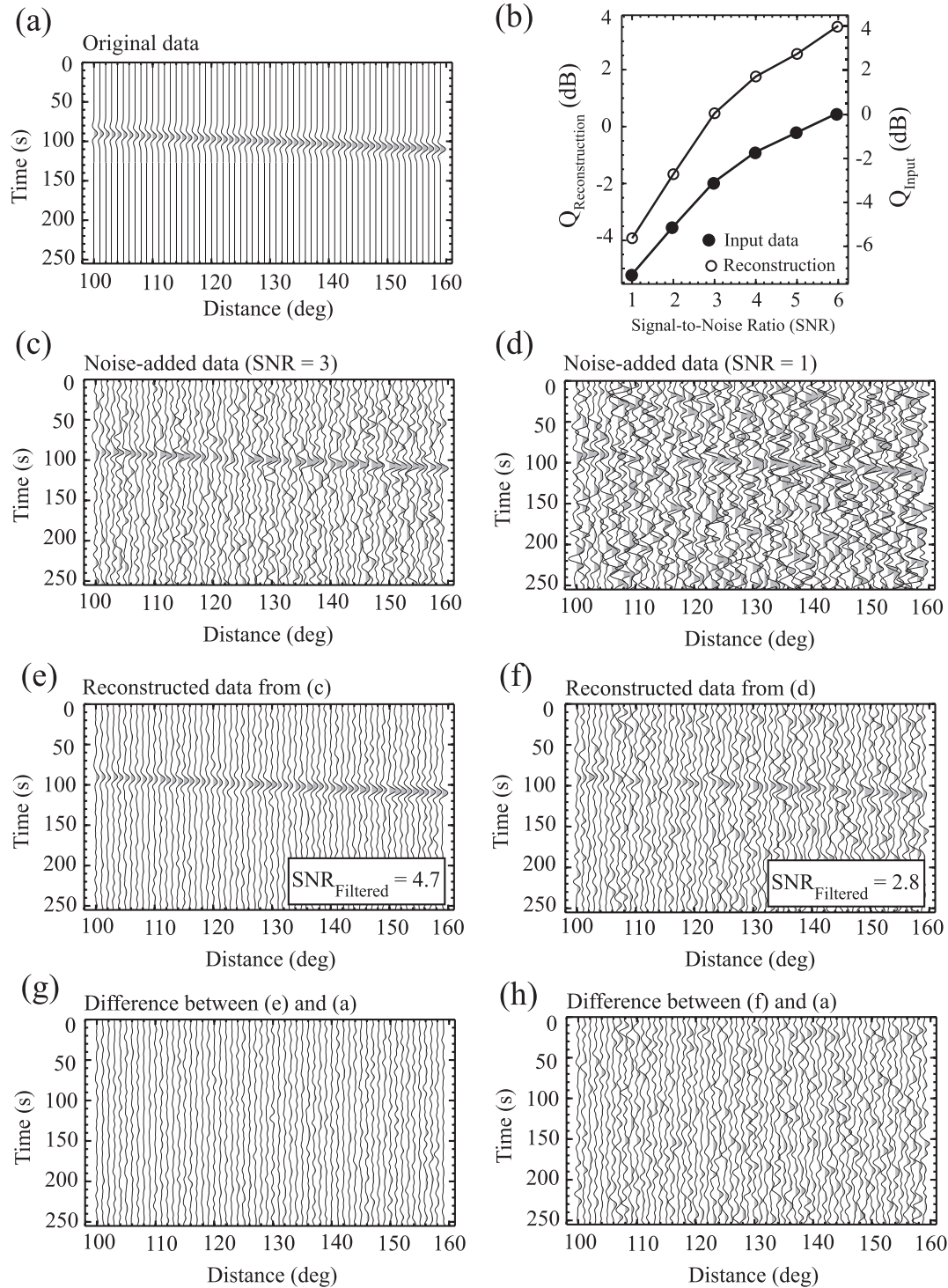


Figure 12. Applications of SSA in filtering data that have been contaminated with additive random noise. (a) Original noise-free data. (b) Quality of the input and filtered data for different SNR values. The filled and open circles show the respective qualities of the input noisy data and the reconstructions. The noise added data with SNR = 3 and 1 are shown in panels (c) and (d), respectively, and their corresponding filtered sections (using $k = 1$) are shown in panels (e) and (f). (g,h) Differences between the filtered and noise-free data.

where SNR after filtering is improved by nearly threefold. Just as importantly, no coherent arrivals are observed on the residual section (Figs 12g and h), which suggest minimal systematic biases during the reconstruction. Further examinations of the α parameter and spurious outliers are provided in the supplementary information (see also Supporting Information Figs S1–S3).

4 CONCLUSIONS

In this study, the upper mantle discontinuities are imaged using SSA, a rank reduction approach that simultaneously removes random noise and reconstructs missing data traces. This method relies on the predictability of mantle conversions and reflections, and it

is implemented in the frequency–space domain. The reconstructed seismic images of the upper mantle show more laterally coherent observations of MTZ discontinuities on both the waveforms of SS precursors and RFs. In addition to consistent MTZ phase boundaries, strong signals near the 520 km discontinuity are successfully identified beneath western Canada and NE China. When utilized properly, this method could be a powerful tool for future analyses of any weak seismic phase from the Earth’s interior. Scripts to perform SSA in the frequency–space domain are presented in Julia, which provides free access to open source libraries and the portability between different platforms (see Appendix A).

ACKNOWLEDGEMENTS

We thank Yunfeng Chen, Ruijia Wang and Simon Schneider for constructive discussions and assistance during the drafting and revision of this manuscript. We also thank Martin Schimmel and two anonymous reviewers for their insightful comments and suggestions. The facilities of IRIS Data Services, and specifically the IRIS Data Management Center, were used for the access to the waveforms, related metadata, and/or derived products used in this study. IRIS Data Services are funded through the Seismological Facilities for the Advancement of Geoscience and EarthScope (SAGE) Proposal of the National Science Foundation under Cooperative Agreement EAR-1261681. This work was supported by the Helmholtz-Alberta Initiative (HAI grant RES0019262) and National Science and Engineering Research Council of Canada (NSERC).

REFERENCES

- Abma, R. & Claerbout, J., 1995. Lateral prediction for noise attenuation by tx and fx techniques, *Geophysics*, **60**(6), 1887–1896.
- Ammon, C.J., Randall, G.E. & Zandt, G., 1990. On the nonuniqueness of receiver function inversions, *J. geophys. Res.*, **95**(B10), 15 303–15 318.
- Auvergne, M., 1988. Singular value analysis applied to phase space reconstruction of pulsating stars, *Astron. Astrophys.*, **204**, 341–348.
- Broomhead, D.S. & King, G.P., 1986. Extracting qualitative dynamics from experimental data, *Phys. D*, **20**(2–3), 217–236.
- Cadzow, J.A., 1988. Signal enhancement-a composite property mapping algorithm, *IEEE Trans. Acoust. Speech Signal Process.*, **36**(1), 49–62.
- Canales, L., 1984. Random noise reduction, in *54th Annual International Meeting*, SEG, Expanded Abstracts.
- Cassidy, J.F., 1995. A comparison of the receiver structure beneath stations of the Canadian National Seismograph Network, *Can. J. Earth Sci.*, **32**(7), 938–951.
- Castle, J.C. & Creager, K.C., 2000. Local sharpness and shear wave speed jump across the 660 km discontinuity, *J. geophys. Res.*, **105**, 6191–6200.
- Chen, K. & Sacchi, M.D., 2015. Robust reduced-rank filtering for erratic seismic noise attenuation, *Geophysics*, **80**, V1–V11.
- Chen, Y. & Ma, J., 2014. Random noise attenuation by f-x empirical mode decomposition predictive filtering, *Geophysics*, **79**, V81–V91.
- Chen, Y., Gu, Y.J., Dokht, R.M. & Sacchi, M.D., 2015. Crustal imprints of Precambrian orogenesis in western Laurentia, *J. geophys. Res.*, **120**(10), 6993–7012.
- Deuss, A., 2009. Global observations of mantle discontinuities using SS and PP precursors, *Surv. Geophys.*, **30**(4–5), 301–326.
- Deuss, A. & Woodhouse, J.H., 2002. A systematic search for mantle discontinuities using SS-precursors, *Geophys. Res. Lett.*, **29**(8), 90-1–90-4.
- Dokht, R.M., Gu, Y.J. & Sacchi, M.D., 2016. Waveform inversion of SS precursors: an investigation of the northwestern Pacific subduction zones and intraplate volcanoes in China, *Gondwana Res.*, **40**, 77–90.
- Dueker, K.G. & Sheehan, A.F., 1997. Mantle discontinuity structure from midpoint stacks of converted P to S waves across the Yellowstone hotspot track, *J. geophys. Res.*, **102**(B4), 8313–8327.
- Dziewonski, A.M. & Anderson, D.L., 1981. Preliminary reference Earth model, *Phys. Earth planet. Inter.*, **25**(4), 297–356.
- Efron, B. & Tibshirani, R., 1990. Statistical data analysis in the computer age, *Science*, **253**, 390–395.
- Flanagan, M.P. & Shearer, P.M., 1998. Global mapping of topography on transition zone velocity discontinuities by stacking SS precursors, *J. geophys. Res.*, **103**(B2), 2673–2692.
- Fraedrich, K., 1986. Estimating the dimensions of weather and climate attractors, *J. Atmos. Sci.*, **43**(5), 419–432.
- Freire, S.L. & Ulrych, T.J., 1988. Application of Singular value decomposition to vertical seismic profiling, *Geophysics*, **53**, 778–785.
- Ghil, M. *et al.*, 2002. Advanced spectral methods for climatic time series, *Rev. Geophys.*, **40**(1), 3–1–3–41.
- Golub, G.H. & Van Loan, C.F., 1996. *Matrix Computations*, 3rd edn, Johns Hopkins Univ. Press.
- Golyandina, N., Nekrutkin, V. & Zhigljavsky, A., 2001. *Analysis of Time Series Structure: SSA and Related Techniques*, Chapman & Hall/CRC Monographs on Statistics & Applied Probability, CRC Press.
- Gu, Y., Dziewonski, A.M. & Agee, C.B., 1998. Global de-correlation of the topography of transition zone discontinuities, *Earth planet. Sci. Lett.*, **157**(1), 57–67.
- Gu, Y.J. & Dziewonski, A.M., 2002. Global variability of transition zone thickness, *J. geophys. Res.*, **107**(B7), ESE 2-1–ESE 2-17.
- Gu, Y.J. & Sacchi, M., 2009. Radon transform methods and their applications in mapping mantle reflectivity structure, *Surv. Geophys.*, **30**(4–5), 327–354.
- Gu, Y.J. & Shen, L., 2015. Noise correlation tomography of Southwest Western Canada Sedimentary Basin, *Geophys. J. Int.*, **202**(1), 142–162.
- Gu, Y.J., Okeler, A., Shen, L. & Contenti, S., 2011. The Canadian Rockies and Alberta network (CRANE): new constraints on the Rockies and western Canada sedimentary basin, *Seismol. Res. Lett.*, **82**(4), 575–588.
- Gu, Y.J., Okeler, A. & Schultz, R., 2012. Tracking slabs beneath northwest Pacific subduction zones, *Earth planet. Sci. Lett.*, **331**, 269–280.
- Gu, Y.J., Zhang, Y., Sacchi, M.D., Chen, Y. & Contenti, S., 2015. Sharp mantle transition from cratons to cordillera in southwestern Canada, *J. geophys. Res.*, **120**(7), 5051–5069.
- Gulunay, N., 1986. FXDECON and complex Wiener prediction filter, in *1986 SEG Annual Meeting*, Society of Exploration Geophysicists.
- Hassani, H. & Thomakos, D., 2010. A review on singular spectrum analysis for economic and financial time series, *Stat. Interface*, **3**(3), 377–397.
- Houser, C., Masters, G., Flanagan, M. & Shearer, P., 2008. Determination and analysis of long-wavelength transition zone structure using SS precursors, *Geophys. J. Int.*, **174**(1), 178–194.
- Kennett, B., 1983. *Seismic Wave Propagation in Stratified Media*, Cambridge Univ. Press.
- Kennett, B. & Engdahl, E., 1991. Traveltimes for global earthquake location and phase identification, *Geophys. J. Int.*, **105**(2), 429–465.
- Kind, R. *et al.*, 1996. Evidence from earthquake data for a partially molten crustal layer in southern Tibet, *Science*, **274**(5293), 1692.
- Kumar, U. & Jain, V., 2010. Time series models (Grey-Markov, Grey Model with rolling mechanism and singular spectrum analysis) to forecast energy consumption in India, *Energy*, **35**(4), 1709–1716.
- Langston, C.A., 1979. Structure under Mount Rainier, Washington, inferred from teleseismic body waves, *J. geophys. Res.*, **84**(B9), 4749–4762.
- Lawrence, J.F. & Shearer, P.M., 2006. A global study of transition zone thickness using receiver functions, *J. geophys. Res.*, **111**, B06307, doi:10.1029/2005JB003973.
- Li, X., Sobolev, S., Kind, R., Yuan, X. & Estabrook, C., 2000. A detailed receiver function image of the upper mantle discontinuities in the Japan subduction zone, *Earth planet. Sci. Lett.*, **183**(3), 527–541.
- Ligorria, J.P. & Ammon, C.J., 1999. Iterative deconvolution and receiver-function estimation, *Bull. seism. Soc. Am.*, **89**(5), 1395–1400.
- Naghizadeh, M., 2012. Seismic data interpolation and denoising in the frequency-wavenumber domain, *Geophysics*, **77**(2), V71–V80.
- Naghizadeh, M. & Sacchi, M., 2013. Multidimensional de-aliased caddow reconstruction of seismic records, *Geophysics*, **78**(1), A1–A5.

- Oropeza, V. & Sacchi, M., 2011. Simultaneous seismic data denoising and reconstruction via multichannel singular spectrum analysis, *Geophysics*, **76**, V25–V32.
- Ringwood, A.E., 1975. *Composition and Petrology of the Earth's Mantle*, McGraw-Hill.
- Rondenay, S., 2009. Upper mantle imaging with array recordings of converted and scattered teleseismic waves, *Surv. Geophys.*, **30**(4–5), 377–405.
- Sacchi, M.D., 2009. FX Singular Spectrum Analysis, *CSPG CSEG CWLS Convention*, 392–395.
- Sacchi, M.D. & Ulrych, T.J., 1995. High-resolution velocity gathers and offset space reconstruction, *Geophysics*, **60**(4), 1169–1177.
- Schaeffer, A. & Bostock, M., 2010. A low-velocity zone atop the transition zone in northwestern Canada, *J. geophys. Res.*, **115**, B06302, doi:10.1029/2009JB006856.
- Shearer, P.M., 1993. Global mapping of upper mantle reflectors from long-period ss precursors, *Geophys. J. Int.*, **115**(3), 878–904.
- Shearer, P.M., 2009. *Introduction to Seismology*, Cambridge Univ. Press.
- Shearer, P.M. & Masters, T.G., 1992. Global mapping of topography on the 660-km discontinuity, *Nature*, **355**(6363), 791–796.
- Song, T.-R.A., Helmberger, D.V. & Grand, S.P., 2004. Low-velocity zone atop the 410-km seismic discontinuity in the northwestern United States, *Nature*, **427**(6974), 530–533.
- Spitz, S., 1991. Seismic trace interpolation in the FX domain, *Geophysics*, **56**(6), 785–794.
- Tauzin, B., Debayle, E. & Wittlinger, G., 2008. The mantle transition zone as seen by global *Pds* phases: no clear evidence for a thin transition zone beneath hotspots, *J. geophys. Res.*, **113**, B08309, doi:10.1029/2007JB005364.
- Trad, D.O., Ulrych, T.J. & Sacchi, M.D., 2002. Accurate interpolation with high-resolution time-variant radon transforms, *Geophysics*, **67**(2), 644–656.
- Trickett, S.R., 2003. F-xy eigenimage noise suppression, *Geophysics*, **68**, 751–759.
- Trickett, S., 2008. F-xy cadzow noise suppression, in *2008 SEG Annual Meeting*, Society of Exploration Geophysicists.
- Trickett, S. & Burroughs, L., 2009. Prestack rank-reduction-based noise suppression, *CSEG Recorder*, **34**(9), 24–31.
- Varadi, F., Pap, J., Ulrich, R., Bertello, L. & Henney, C., 1999. Searching for signal in noise by random-lag singular spectrum analysis, *Astrophys. J.*, **526**(2), 1052–1061.
- Vautard, R. & Ghil, M., 1989. Singular spectrum analysis in nonlinear dynamics, with applications to paleoclimatic time series, *Phys. D*, **35**, 395–424.
- Vinnik, L., 1977. Detection of waves converted from P to SV in the mantle, *Phys. Earth planet. Inter.*, **15**(1), 39–45.
- Wicks, C.W. & Richards, M.A., 1993. A detailed map of the 660-kilometer discontinuity beneath the Izu-Bonin subduction zone, *Science*, **261**(5127), 1424–1427.
- Yang, H.H. & Hua, Y., 1996. On rank of block Hankel matrix for 2-D frequency detection and estimation, *IEEE Trans. Signal Process.*, **44**(4), 1046–1048.
- Yuan, S. & Wang, S., 2011. A local *f-x* Cadzow method for noise reduction of seismic data obtained in complex formations, *Pet. Sci.*, **8**, 269–277.
- Zheng, Z., Ventosa, S. & Romanowicz, B., 2015. High resolution upper mantle discontinuity images across the Pacific Ocean from SS precursors using local slant stack filters, *Geophys. J. Int.*, **202**(1), 175–189.

SUPPORTING INFORMATION

Supporting information is available at [GJIRAS](#) online.

Figure S1. Application of SSA when arrivals are locally delayed by 5 s. (a) Input data. (b), (d) and (f) Reconstructed data using $k = 1$ and $\alpha = 0.2, 0.4$ and 0.6 , respectively. (c), (e) and (g) The corresponding differences between the reconstructed and input data. The dashed box outlines the time-shifted signals.

Figure S2. Effect of large amplitude arrivals on the SSA interpolated data. (a) Original data consisting of two linear events. The steeper event shows higher amplitude signals in the middle of section. (b) Decimated input data. (c) and (e) Reconstructed images using $\alpha = 0.4$ and 0.8 , respectively. Only the first two singular values are used to reconstruct the data. The average amplitude recovery of the missing traces is shown on the reconstructed sections. (d) and (f) Differences between the SSA interpolated and original data.

Figure S3. Effect of a high amplitude outlier on the SSA reconstructed results. (a) Input section containing two linear events with a large amplitude outlier in between. (b), (c) and (d) The SSA interpolated sections using $k = 2$ and $\alpha = 0.2, 0.4$ and 0.6 , respectively. The amplitude recovery of the input outlier is shown on the reconstructed sections. (e), (f) and (g) The corresponding differences between the interpolated and input data.

Please note: Oxford University Press is not responsible for the content or functionality of any supporting materials supplied by the authors. Any queries (other than missing material) should be directed to the corresponding author for the paper.

APPENDIX A: SUPPLEMENTARY MATERIALS

Supplementary codes and data associated with this paper can be found at:

<https://sites.ualberta.ca/~ygu/projects/ssa/>.